MODELING AND SIMULATION OF A SUPERCRITICAL CO2-LIQUID SODIUM COMPACT HEAT EXCHANGER FOR SODIUM FAST REACTORS

Hailei Wang[1,*] and Sean M. Kissick[2]

[1]Department of Mechanical and Aerospace Engineering
4130 Old Main Hill, Utah State University
Logan, UT 84321

[2]Energy Storage Systems, Wilsonville, OR 97070

([*] Correspondence Author Email: hailei.wang@usu.edu)

ABSTRACT

The study focuses on modeling and simulations of sodium-sCO2 intermediary compact heat exchangers for sodium fast reactors (SFR). A simplified 1-D analytical model was developed in companion with a 3-D CFD model. Using classic heat transfer correlations for Nusselt number, some simulation results using the 1-D model have achieved reasonable match with the CFD simulation results for longer channels (i.e., 40 cm and 80 cm). However, for short channel (10 cm) when axial conduction within the sodium fluid is significant, the 1-D model significantly over-predicted the heat transfer effectiveness. By incorporating the temperature-jump model, the 1-D model can extend its predictive capability for low-Prandtl number fluid/Peclet number flows. The results can help improve the understanding of heat transfer for sodium and low-Prandtl number fluids in general and improve designs of sodium-sCO2 compact heat exchangers. The results also confirmed that the sCO2 side dominates the overall heat transfer for Na-sCO2 heat exchangers. A preliminary attempt of optimizing the channel geometry shows mixing results – while heat transfer effectiveness was significantly increased for the wavy channel, much greater pressure drop was also predicted by the simulations.

KEYWORDS: Sodium Fast Reactor, Compact Heat Exchanger, Supercritical CO2, CFD, Low-Prandtl Number, Axial Conduction, microchannel

NOMENCLATURE

A	*Heat transfer surface area [m2]*
Cp	*Specific Heat Capacity of fluid [kJ/kg-K]*
k	*Thermal conductivity of heat exchanger material [W/m-K]*
$\dot{m}$	*Fluid mass flow rate [kg/s]*
Nu	*Nusselt number*
Pe	*Peclet number*
Pr	*Prandtl number*
Re_D	*Reynolds number (channel hydraulic diameter as characteristic length)*
R_T	*Total thermal resistance of 1-D heat transfer model [K/W]*
L	*Total length of the channel [m]*
t	*thickness of channel wall [m]*
T	*Temperature [˚C]*
U	*Average fluid velocity [m/s]*
u	*Local fluid velocity in the x-direction [m/s]*
v	*Local fluid velocity in the y-direction [m/s]*
w	*Local fluid velocity in the z-direction [m/s]*
x	*Direction perpendicular to the fluid channel and side of channel [m]*
y	*Direction perpendicular to the fluid channel and base of channel[m]*
z	*Direction transverse to the fluid channel [m]*
Δq	*Heat transfer between fluids within a discretized channel section*
θ	*Non-dimensional temperature*

Subscripts

b	*Bulk fluid*
c	*Cold fluid*
h	*Hot fluid*
i	*Inlet*
o	*Outlet*
Na	*Liquid Sodium*
$sCO2$	*Supercritical CO2*
$wall$	*Heat exchanger wall*

Superscripts

j	*Index for discretized section*
$*$	*Non-dimensional value*

1. INTRODUCTION

Nuclear energy has been gaining renewed interest with research into the generation IV advanced nuclear reactors, with the promise of improved safety, sustainability and economics [1]–[4]. Within the six proposed Gen IV reactor designs, sodium-cooled fast reactors (SFR) are well positioned to be deployed between year 2020 and year 2030 owing to the significant past experience accumulated with sodium cooled reactors in several countries [5]–[9]. According to a summary of SFR status in 2014 by Aoto et al. [10], development of SFR has been advanced to becoming the first Generation-IV system which is dedicated to sustainable energy generation and actinide management. Currently, several advanced SFR concepts and designs are under development worldwide.

The sodium-cooled fast reactor system uses liquid sodium as the reactor coolant, allowing high power density with low coolant volume fraction, as well as great thermal and safety properties [11], [12]. Over the past ten years, experimental reactors have demonstrated the inherent safety of advanced sodium cooled fast reactor designs [13]. SFRs also feature a closed fuel cycle for fuel breeding and better actinide management. As a liquid metal, sodium has very low vapor pressure. Essentially there is little to no pressure within the reactor core, unlike typical light-water reactors operating over 100 bars [14], [15]. Sodium, as a low-Prandtl number fluid, also possesses extremely high thermal conductivity which can be up to 100 times greater than typical fluids used in heat exchangers [16], [17]. If designed properly, this important fluid characteristic can also provide potential advantage of higher heat transfer rates to the secondary working fluids over current water-cooled reactors [18].

Characterized by Prandtl numbers much less than 1, sodium exhibits significantly higher thermal diffusivity compared to momentum diffusivity. Several numerical studies have been conducted in recent years to improve understanding of thermal transport of low-Prandtl number fluids such as sodium, including direct numerical simulation [19], [20], large eddy simulation [21] and RANS with improved near-wall modeling [22]. However, the challenges remain in designing and optimizing sodium secondary

heat exchangers due to lack of reliable methods to accurately and computational-efficiently model heat transfer in liquid sodium [23], [24]. This is due to conduction heat transfer in low-Prandtl number fluids can be significant compared to convection heat transfer. As a result, axial conduction (commonly ignored for other fluids) within sodium can greatly affect thermal performance, especially when targeting high heat transfer effectiveness for compact heat exchangers [25], [26]. According to Parahovnik et al. [27], using a modified NTU approach that includes axial conduction effect significantly reduce the discrepancy between model predictions and experimental data.

Being highly reactive with water, sodium imposes an operating concern when coupling sodium fast reactors with steam Rankine cycles. In recent years, intensive research on Generation IV advanced nuclear reactors is looking to couple a sodium fast reactor with a closed supercritical CO2 (sCO2) Brayton cycle in place of standard steam Rankine cycles [28]–[30]. In doing so, it not only helps mitigate potential safety concerns [31], but also achieve potentially higher cycle temperature and associated efficiencies [32]. According to Park et al. [33], the optimized cycle efficiency for a sodium fast reactor and a high temperature gas reactor can reach 46.38% and 50.04%, respectively. The cycle thermal efficiency was improved by using printed circuit heat exchangers (PCHEs), especially with the airfoil fin type channel design. Operating around supercritical condition where the density of sCO2 spikes, the power required to compress sCO2 is also greatly reduced leading to further cycle efficiency improvement [34]. In addition, the size of the sCO2 turbines is drastically reduced compared to steam turbines resulting in better economics [35]–[37].

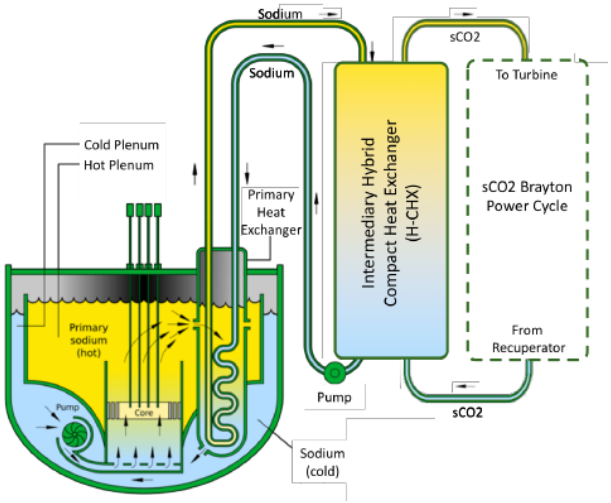

FIGURE 1: Schematic of a sodium fast reactor coupled with an intermediary hybrid compact heat exchanger which transfers heat from the liquid sodium to the supercritical CO2 within a closed Brayton cycle. Image is adapted from Wiki Commons.

Unlike sodium, however, supercritical CO2 has very poor thermal conductivities. This mismatch imposes great challenges for designing high-performance, low-cost and compact sodium-sCO2 heat exchangers. Convective heat transfer on the supercritical CO2 side is expected to dominate the overall thermal resistance between sodium and supercritical CO2 [38]. Both experimental and numerical investigations on forced convection heat transfer of supercritical carbon dioxide in a prototypic printed circuit heat exchanger was conducted by Li et al. [39]. Good agreement was found between the experiments and FLUENT simulations using an SST k–w model with the near-wall region being completely resolved. Furthermore, experimental and computational data were compared to empirical predictions by the Dittus–Boelter and Jackson correlations. The results showed that Dittus–Boelter correlation has better precision for the average value of the predicted heat transfer coefficient than the Jackson correlation which overestimates the average value of heat transfer coefficient in the whole range of the experiment conditions. However, Jackson correlation considers the heat flux effect by properly accounting for thermophysical property changes in the radial direction, resulting in better local predictions. The authors proposed a new correlation evaluated by PDF-based time-averaged properties for forced convection heat transfer of supercritical CO2 in both heating and cooling mode.

Thus, heat transfer enhancement within supercritical CO2 channels is likely needed for technology deployment [40], [41]. Microchannel heat exchangers have been shown to greatly enhance heat transfer given its short diffusion length scale and large surface area per volume ratio, which enables both volume- (kW/m3) and mass-based (kW/kg) power densities. As a result, microchannel-based hybrid compact heat exchangers (H-CHX) have been identified for supporting sodium fast reactors [42]–[47]. To transfer heat from the sodium to the supercritical CO2, an intermediary (secondary) heat exchanger is required in which the sCO2 is heated by cooling the sodium prior to its return to the reactor (Figure 1).

In this study, a 1-D model for the intermediary heat exchanger was firstly developed, which was followed by a 3-D CFD model. Given significant differences were observed between the 1-D and CFD models at short heat exchanger lengths (e.g. 10 cm), the analytical temperature-jump model was also developed to capture the excessive axial conduction within the sodium. The goal is to use the models to accurately simulate the steady-state operation within the intermediary heat exchanger channels for typical operating conditions in a sodium fast reactor. The predicted solid temperature profiles were also provided as inputs for thermo-mechanical modeling of the sodium-sCO2 intermediary heat exchanger. This paper briefly introduces the heat exchanger design, while mainly focuses on discussing the development of the models and the results of the simulations. The result of preliminary investigation of channel geometry is also presented. Future research on the Na-sCO2 H-CHX will be focused on optimizing channel size and geometry (straight, zig-zag, air foil channels) with respect to thermal performance, pressure drop, cost, and manufacturability.

Table 1: An example of intermediary Na-sCO2 heat exchanger operating condition for SFR

Parameter	Value
sCO2	
Inlet Temperature	$350°C$ [1]
Outlet Temperature	$520°C$ [1]
Pressure	20-25 MPa [2]
Liquid Sodium	
Inlet Temperature	$550°C$ [1]
Outlet Temperature	$380°C$ [1]
Pressure	0 MPa (gauge) [1]

2. DESIGN AND MODELING

2.1 Heat Exchanger Design

For the H-CHX intermediary heat exchanger, its inlet and outlet temperatures were selected based on the work from Cha et al. [48]. It provided the operating specifications of the power cycle for a 600 MWe sodium fast reactor as shown in Table 1. The inlet operating temperature for the sodium is 550 °C while the operating inlet pressure for the sCO2 is 25 MPa [49]. Design considerations for the intermediary heat exchanger is to achieve a high sCO2 exit temperature by matching the temperature profile of the sodium while maintaining low pressure drops for both fluids in order to minimize the power consumption of sodium pump and sCO2 compressor. Given the extreme pressure differences between the sCO2 and sodium sides, mechanical design of the heat exchanger was carefully addressed using the mechanical model developed by Heatric [50]. The wall thickness of the heat exchanger was determined under static pressure loading conditions, in which the pressures for the sCO2 was at 25 MPa while the Na operates near atmospheric pressure. The heat exchanger material chosen was SS-316. As shown in Figure 2, the sCO2 side of the model is based on the standard cross-sectional profile after a typical photochemical etching process.

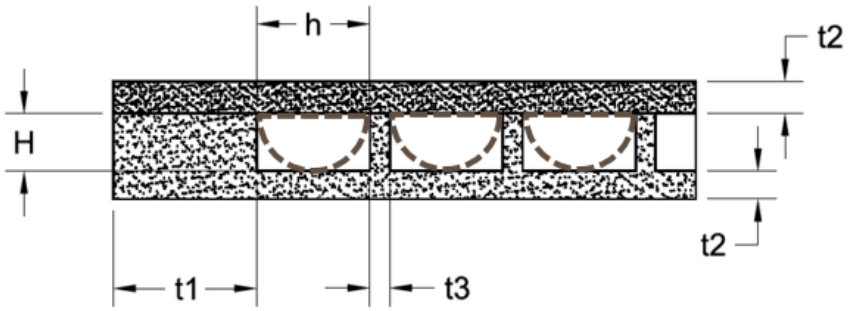

Figure 2: Showing the semi-circles associated with photochemical etching process and the key dimensional variables for the sCO2 side [13].

The key dimensions for the heat exchanger are listed in Table 2. The diameter of the sCO2 channel was selected based off the optimization work from Ishizuka et al. [51]. It worth mentioning the table included three Na channel designs: 1) the original rectangular cross-sectional design for Na channels; 2) the modified rectangular cross-sectional design for Na channels; 3) the final semi-circle cross-sectional design for Na channels, which shares the same cross-sectional dimensions as the sCO2 channels. In addition, the study also conducted a preliminary investigation on a wavy channel (instead of straight channel for designs mentioned above) with the same cross-section as the semi-circle design.

The Na channel was initially modeled with a rectangular cross-section with the height five times of the sCO2 channel and spans two sCO2 channels as shown in Figure 3(a). The intention was to minimize sodium pumping power. However, the study quickly found that large open rectangular channel for sodium resulted in low flow velocity, which induced substantial axial conduction within the fluid itself causing poor thermal performance for short channel designs. Heat transfer effectiveness has been improved significantly by reducing Na channel size by half (shown in Figure 3(b)). To further study the trend, the final design of the Na channel shared the same shape and dimensions as the sCO2 channel shown in Figure 3(c).

Table 2 – The hybrid compact heat exchanger channel designs – including: 1) the original Na channel design using rectangular; 2) the modified Na channel design using semi-circle

Parameter	**Original** Na Channel Design (Rectangular)	**Modified** Na Channel Design (Rectangular)	**Final** Na Channel Design (Semi-circle)
sCO2 channel diameter, h	1.90 mm	1.90 mm	1.90 mm
sCO2 channel height, H	0.90 mm	0.90 mm	0.90 mm
Na channel width/diameter	4.06 mm	**4.06 mm**	**1.90 mm**
Na channel height	9.00 mm	**4.50 mm**	**0.90 mm**
Na/sCO2 wall thickness, t2	1.03 mm	1.03 mm	1.03 mm
Fin thickness, t3	0.26 mm	0.26 mm	0.26 mm
Wavy channel amplitude	0.40 mm	0.40 mm	0.40 mm
Wavy channel wavelength	5.50 mm	5.50 mm	5.50 mm

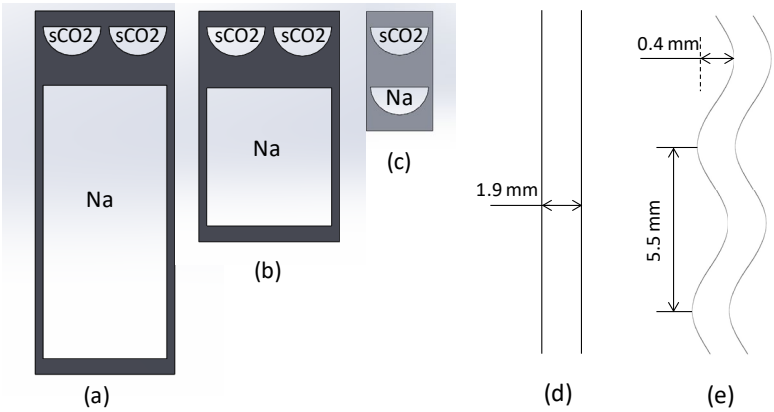

FIGURE 3: (a) Initial unit-cell design for a diffusion bonded H-CHX channels; (b) Modified unit cell design; (c) Final unit cell design; (d) Final design – straight channel; (e) Wavy channel

The operating conditions shown in Table 1 were used to run the 1-D model first. Given fixed inlet and outlet temperatures for each fluid, the mass flow rates of sodium and sCO2 were calculated for different channel lengths. To compare with the 3-D simulation, the mass flow rates determined from the 1-D model were used as the simulation inputs for the 3-D CFD model on the same channel design. It then predicts the outlet temperatures of both fluids and their streamwise temperature profiles. Details of the 1-D and 3-D CFD models are discussed in the following sections.

2.2 The 1-D Model

The 1-D model considers only 1-D (transverse) heat transfer between the fluids, which is the standard approach for heat exchanger analysis. For a given set of fluid inlet temperatures and heat transfer

effectiveness, the model computes the mass flow rate for each fluid and fluid outlet temperatures. Unlike conventional heat exchanger analysis, the model also discretizes the fluid domain in the stream-wise direction into N sections with spacing of Δx. This allows the 1-D model to solve the entire temperature profile along the channels. In addition, it allows the model to capture the temperature-dependency of fluid properties, especially around the supercritical point of carbon dioxide. As shown in the zoom-in section in Figure 4, a resistance network model is implemented to compute the heat transfer between the two fluids. Coupled with the energy balance equation for each fluid, the heat transfer equation between the two fluids computes the outlet temperatures of the fluids for each discretized section. The process starts from the inlet of each fluid to find the entire stream-wise temperature profile for each fluid. The equations governing the 1-D model are given below:

$$\Delta q = (\dot{m}C_p)_{sCO2}(T^j_{o,sCO2} - T^j_{i,sCO2}) \tag{1}$$

$$-\Delta q = (\dot{m}C_p)_{Na}(T^j_{o,Na} - T^j_{i,Na}) \tag{2}$$

$$\Delta q = \frac{T^j_{b,Na} - T^j_{b,sCO2}}{R_T} \tag{3}$$

$$R_T = \frac{1}{(hA)_{Na}} + \frac{t}{kA} + \frac{1}{(hA)_{sCO2}} \tag{4}$$

$$T^j_b = \frac{T^j_i + T^j_o}{2} \tag{5}$$

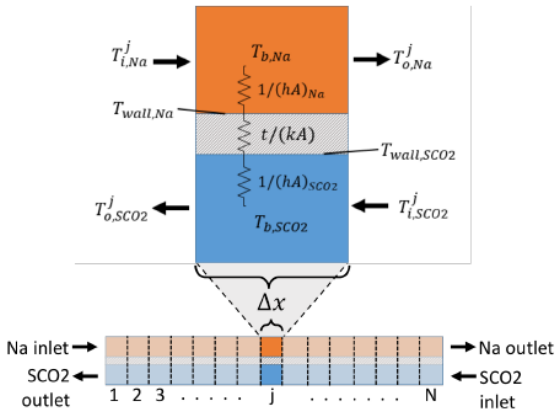

FIGURE 4: Discretization of H-CHX for use in 1-D heat transfer model. Each discretized section uses a thermal resistance model to find the sectional outlet temperatures and flow rates.

In the 1-D model, two classic heat transfer correlations for Nusselt number were used to determine convection coefficients for sCO2. For laminar sCO2 flow, a constant heat flux Nusselt correlation (Eqn. 6) for semi-circle channels was selected [52]. For turbulent sCO2 flow, a modified Dittus-Boelter correlation (Eqn. 7) was employed according to [53]:

$$Nu_D = 4.089 \qquad (6)$$

$$Nu_D = 0.14 Re_D^{0.69} Pr^{0.66} \qquad (7)$$

To determine the convection coefficient for liquid sodium, the Seban-Shimazaki correlation (Eqn. 8) developed for liquid metals was used for predicting Nusselt number [54][16]. It is an empirical model that accounts for the high thermal conductivity of the liquid sodium.

$$Nu_D = 5.0 + 0.025(Re_D Pr)^{0.8} \qquad (8)$$

The 1-D model was developed in MATLAB, which also incorporated temperature-dependent fluid properties. To run the simulation with specified inlet and outlet temperatures, the initial flow rates for both fluids were guessed in order to solve for the internal temperatures within the heat exchanger channels. The simulation solved equations 1-5 at each Δx and iterated through until the residual values (the difference between the current temperature solution with the previous temperature solution) reached

a maximum absolute residual value of 1e-6 for all solved temperatures. Outlet temperatures were then compared, and fluid flow rates were iteratively changed using an optimization algorithm until the model outlet temperatures were within 1% of the target fluid outlet temperatures according to the defined heat exchanger effectiveness. The detailed solution algorithm is illustrated in Figure 5.

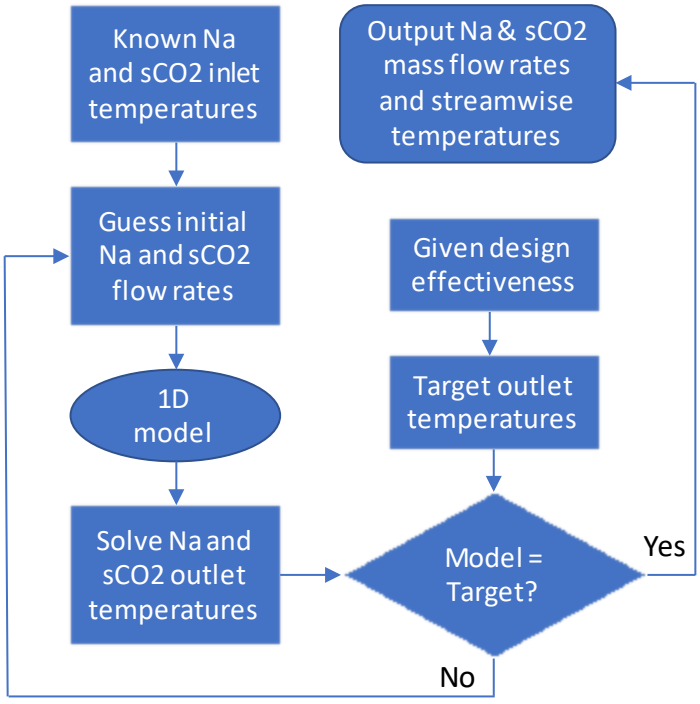

FIGURE 5: Solution steps for the 1-D model to find the mass flow rates and stream-wise temperature profile.

2.3 The 3-D CFD Model

In order to validate the simplified 1-D model and better capture all the physics within each fluid with less assumptions, a 3-D CFD model was developed using ANSYS FLUENT 15.0.7 to solve the Navier-Stokes equations for each fluid and the energy equations within both fluids and solid. As one of the key motivations in this study, properly modeling heat transfer in low-Prandtl number fluids like sodium will be valuable in improving Na-sCO2 intermediary heat exchanger designs. The non-dimensional energy equation for sodium and sCO2 is shown in Eqn. 9, wherein $\theta = (T-T_c)/(T_h-T_c)$, $u^* = u/U$, $v^* = v/U$, $w^* = w/U$, $x^* = x/L$, $y^* = y/L$, *and* $z^* = z/L$.

$$u^*\frac{\partial\theta}{\partial x^*}+v^*\frac{\partial\theta}{\partial y^*}+w^*\frac{\partial\theta}{\partial z^*}=\frac{1}{Pe}\left(\frac{\partial^2\theta}{\partial x^{*2}}+\frac{\partial^2\theta}{\partial y^{*2}}+\frac{\partial^2\theta}{\partial z^{*2}}\right) \quad (9)$$

As shown in Eqn. 9, the non-dimensional Peclet number (Pe = RePr), which measures the relative magnitude of the convection transport rate over the conduction transport rate, plays a critical role for liquid sodium. With typical Prandtl number around 0.004 in typical SFR operating conditions, the sodium side will experience very low Peclet numbers, especially at low mass flow rates (associated with shorter channel length). The inverse of the low Peclet number can amplify the heat conduction terms on the right-hand side of Eqn. 9 and significantly change the temperature profile in liquid sodium. Given the 1-D model ignores the stream-wise heat conduction term which is affected by the low-Peclet number in Eqn. 9, the heat conduction effect within sodium will not be captured in the model.

Details on the CFD physics models, discretization schemes, meshing methods, boundary conditions, and solution converge criteria are discussed in the following subsections.

Physics Model. Due to mass flow rates are changed greatly for the simulations resulting in laminar and turbulent flow regimes, the CFD model used the SST k-ω turbulence model with low-Re correction. The SST k-ω has been shown as a better predictor than other models as it does not use standard wall functions, which allows it to better capture the conditions at the near wall region [53],[54]. The mass, momentum, and energy equations used the QUICK scheme, while the pressure and velocity coupling employed the SIMPLEC algorithm. Fluid properties where determined as a function of temperature only, as pressure variations are relatively small within the domain. The thermophysical data of sCO2 was provided by the NIST Standard Reference Database [57], while the Na data used the work from Argonne National Lab [58].

Meshing. Model geometries were meshed using ANSYS Meshing as shown in Figure 6 – the left image reflects the modified rectangular channel design for sodium while the right image depicts the semi-circle channel design for both fluids. Each mesh includes most hexahedral elements within the fluid regions

with prism layers close to the wall in order to resolve the boundary layers. In order to keep the non-dimensional y+ value of 1 or less being reached at the near wall locations for the SST k-ω model, the prism cells layers growth and sizing were adjusted for each simulation. The solid region of the heat exchanger (walls) contained relatively coarse meshes, while the sodium and supercritical CO2 regions had finer mesh, respectively.

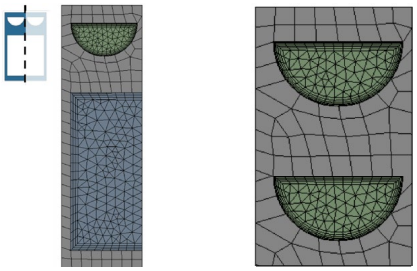

FIGURE 6: (left) Unit cell mesh using rectangular channel for liquid sodium; (right) Unit cell mesh using semi-circle channel for liquid sodium.

Boundary Conditions. Fluid regions boundaries used uniform velocity, iso-thermal inlets, and pressure outlets. Additionally, the unit cell shown in Figure 3 (b) was cut in half and a symmetry boundary condition was applied to both the fluid and solid domains to reduce mesh cell count as shown in Figure 6 (left). The boundaries for the solid heat exchanger walls employed a periodic condition on the top and bottom, while symmetry is placed on the sides and adiabatic is placed on the front and back. To compare the 1-D model to the 3-D model, the uniform velocity at the inlets were determined by using the mass flow rates computed during the 1-D simulation for a given channel length.

Residuals. All equations were solved with absolute residuals less than 1e-5 for all mass, momentum, and turbulence equations, and 1e-7 for the energy equation. Absolute residuals were determined by taking the maximum absolute value of the previous solutions minus the current solutions.

Grid Independence. To understand how grid/mesh sizing influenced the results, a Grid Convergence Index (GCI) study was performed on the 40-cm length channel for the outlet temperatures of both fluids and wall heat transfer [59]. The GCI showed grid errors of less than 1% with an apparent order of accuracy greater than 2 for the mesh size implemented in the CFD models.

2.4 The Temperature-Jump Model

Given the relatively high computational cost associated with the CFD model, a temperature-jump model typically used to capture axial conduction within heat exchanger walls was developed in order to include and assess the effects of axial conduction within sodium. With approximately balanced heat exchanger design, the temperature-jump model is used to estimate the axial conduction rate due to sodium alone. The model essentially computes the 1D heat conduction within the sodium from the inlet to outlet according to the following thermal resistance equation:

$$\dot{q}_{AC} = \frac{T_{HI} - T_{CI}}{R_{AC}} \tag{10}$$

Wherein T_{HI} is the sodium inlet temperature, T_{CI} is the sCO2 inlet temperature, R_{AC} is the thermal resistance within sodium from its inlet to outlet as:

$$R_{AC} = \frac{L_{HX}}{k_{Na} A_c} \tag{11}$$

L_{HX} is the length of the channel for the sodium-sCO2 heat exchanger, k_{Na} is the thermal conductivity of liquid sodium, A_c is the cross-sectional area of the sodium channel. A temperature-jump model typically assumes the hot fluid entering the heat exchanger transfers thermal energy to the wall at a rate that is equivalent to the axial conduction rate. In this case, instead of occurring in the heat exchanger walls, the axial conduction predominantly happens within the sodium – this is because the thermal conductivity of sodium is 4X that of the heat exchanger wall using SS 316 and the cross-sectional area of the sodium channel is much greater than that of the channel wall. Thus, the magnitude of the temperature jumps at the fluid inlets is modeled as follows:

$$\dot{C}_H (T_{HI} - T^*_{HI}) = \frac{T^*_{HI} - T^*_{CI}}{R_{AC}} \tag{12}$$

$$\dot{C}_C (T^*_{CI} - T_{CI}) = \frac{T^*_{HI} - T^*_{CI}}{R_{AC}} \tag{13}$$

Wherein the $(T_{HI} - T_{HI}^*)$ and $(T_{CI}^* - T_{CI})$ represent the temperature jumps at the sodium and sCO2 inlet, respectively. T_{HI}^* and T_{CI}^* become the predicted (actual) sodium and sCO2 inlet temperature in the temperature-jump model. In a typical heat exchanger design, the maximum heat transfer is governed by:

$$\dot{q}_{max} = \dot{C}_{min}(T_{HI} - T_{CI}) \qquad (14)$$

It can be used to define an axial conduction parameter, λ, which provides the magnitude of axial conduction relative to the overall heat transfer potential between the two fluids.

$$\lambda = \frac{\dot{q}_{AC}}{\dot{q}_{max}} \qquad (15)$$

3. RESULTS AND DISCUSSIONS

In this study, while significant efforts were made to develop the 1-D analytical and 3-D CFD models in order to accurately capture the physics within both sodium and supercritical CO2 heat transfer, substantial insights have also been learned though comparing the predictions of the two models. Current simulations have been focusing on the effects of 1) channel length; and 2) mass flow rate on the heat transfer effectiveness for a pair of Na and sCO2 channels (i.e. Unit Cell). To keep the section concise while representing the trend identified, only the simulation results for the modified Na channel design (short rectangular) and final Na channel design (semi-circle) are presented. As a preliminary design optimization study for channel geometry, the result of 10 cm wavy channel is also compared with the same length straight channel design. While the effect of axial conduction within sodium is not readily visible in longer channels, significant impact on short channels is evident in the following figures.

3.1 Effect of Channel Length

Three-channel length of 10, 40 and 80 cm were investigated in order to understand the extent of axial conduction within sodium. In order to keep the inlet and outlet temperatures of sodium and sCO2 as shown in Table 1 (essentially a given heat transfer effectiveness), the mass flow rate of each fluid was also increased as the channel length was increased. As the CFD simulation inputs, the mass flow rates for

both fluids were calculated in the 1-D model first. The key outputs of the CFD simulations are the fluid temperature profiles along the channel length and the values at the outlets. For 10 cm channel, the results from both models are plotted in Figure 7, which shows the bulk temperature profiles of the two fluids change along the length of channel. In this case, the liquid sodium and supercritical CO2 mass flow rate is 1.060e-5 kg/s and 1.07e-5 kg/s respectively, corresponding to Peclet number of 0.086 for sodium flow. As shown, there is a sizeable discrepancy between the 1-D and CFD simulations. At the inlet of sodium (left side of the CFD plot), the Na temperature drops instantly from the inlet temperature of 550 °C to roughly 520 °C. At the same time, a rapid rise in temperature of the sCO2 takes place at its inlet (right side of the plot). As attributed to the short conduction path (10 cm), energy from the Na fluid entrance is axially conducted to heat the cold sCO2 fluid entering the channel. While the rapid drop in temperature was not captured by the simplified 1-D model, it becomes apparent that at low-Peclet numbers, heat exchanger effectiveness will likely suffer as the upstream flow will enter the heat exchanger at a lower temperature according to the 3-D CFD simulation.

Similar result (sudden change of fluid temperatures at the inlets) predicted by the CFD model is obtained after incorporating the temperature-jump model (described in detail in Section 2.4) with the 1-D model. As the model predicts, the predicted actual sodium and sCO2 inlet temperatures become 519 °C and 382 °C, respectively. It shows the axial conduction has caused substantial drop on heat transfer effectiveness and the result matches well with the 3D CFD results shown in Fig. 7. Like the CFD results shown in the next, the axial conduction modeled by the temperature-jump model has shown almost no effects on either the 40 cm or 80 cm channels. This is because the combination of increased channel length (i.e. stream-wise thermal resistance) and sodium mass flow rate (i.e. the heat capacity of the sodium), which corresponds to substantial increase in overall heat transfer rate between the sodium and supercritical CO2 while the amount of axial conduction remains the same.

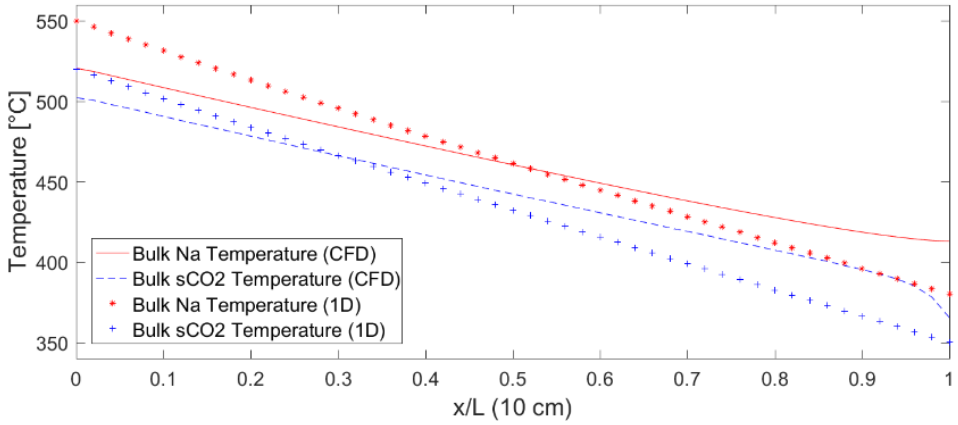

FIGURE 7: Temperature profiles of liquid sodium and supercritical CO2 – 10 cm length channel

Figure 8 shows the fluid temperature profiles for 40 cm channel. In order to reach similar outlet temperatures, the liquid sodium and supercritical CO2 mass flow rates were increased to 1.49e-4 kg/s and 1.51e-4 kg/s respectively. The Na Peclet number was increased to 1.2. With increase in both channel length (axial thermal resistance) and mass flow rate (overall heat transfer for given inlet and outlet temperatures), difference between the two models is much reduced with 1-D model still slightly over-predict the heat transfer effectiveness.

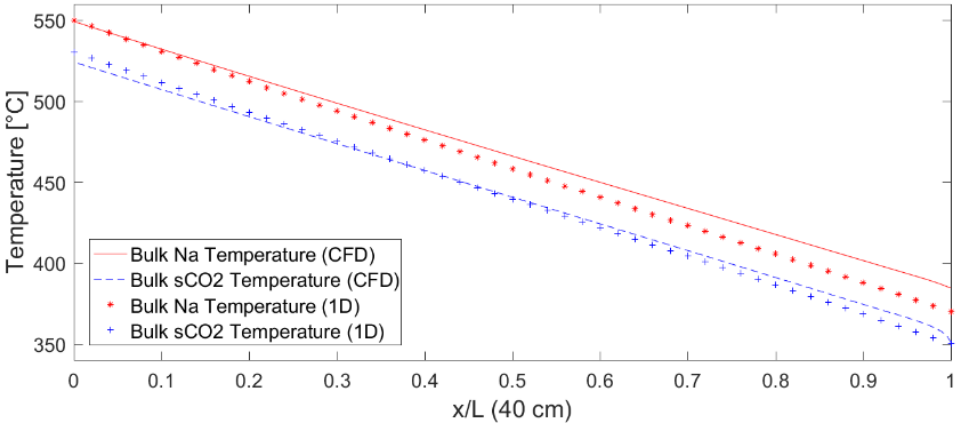

FIGURE 8: Temperature profiles of liquid sodium and supercritical CO2 – 40 cm length channel

Similar plots are also obtained for 80 cm channel as shown in Figure 9, in which case the flow rates for sodium and supercritical CO2 were increased to 1.49e-3 kg/s and 1.52e-3 kg/s respectively. The Na Peclet number reached 12. It should be noted, for the 80 cm channel, only the last 20 cm of the channel towards

the inlet of supercritical CO2 was simulated with CFD in order to reduce computational resources. The inlet temperature for the sodium was determined from running an 80 cm 1-D simulation where the sodium temperature at the 60 cm mark in the channel was selected as the inlet temperature for the CFD simulation. Similarly, the CFD model shows slightly lower effectiveness than the 1-D model in the 80 cm channel. For all three cases, larger temperature gradient at the sCO2 entrance (x/L = 1) is identified, which is benefited from the development of the boundary layers. More details about the entrance effect is presented in the Section 3.2 about Nusselt number.

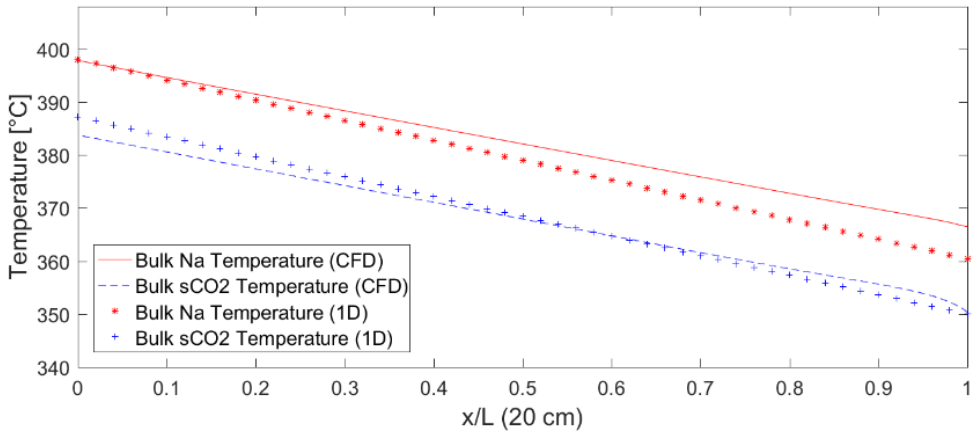

FIGURE 9: Temperature profiles of liquid sodium and supercritical CO2 – 80 cm length channel

3.2 Nusselt Number

With the CFD model showing a nonlinear temperature profile at the sCO2 entrance (right side of the plots) for all channel lengths, the Nusselt numbers along channel length are plotted in Figures 10-12. As shown, the Nusselt number is clearly a function of position for all three channel lengths especially next to the sCO2 inlet showing the entrance effect. In contrast, the 1-D model did not account for the entrance effect. As the sCO2 fluid is in laminar flow regime for the 10 cm channel as mass flow rate is the lowest, it enters the transition regime for the 40 cm channel, and turbulent regime for the 80 cm channel. As the mass flow rate of the sCO2 increases from the laminar to turbulent regime, the Nusselt number increases almost 7 folds as shown in the figures. In contrast, the liquid sodium is laminar for the 10 cm and 40 cm channel lengths and enters transitional regime for the 80 cm length. According to the plots, the Nusselt

number for sodium shows little change for all channel lengths. Overall, the Nusselt number graphs show reasonable agreement between the 1-D and CFD models.

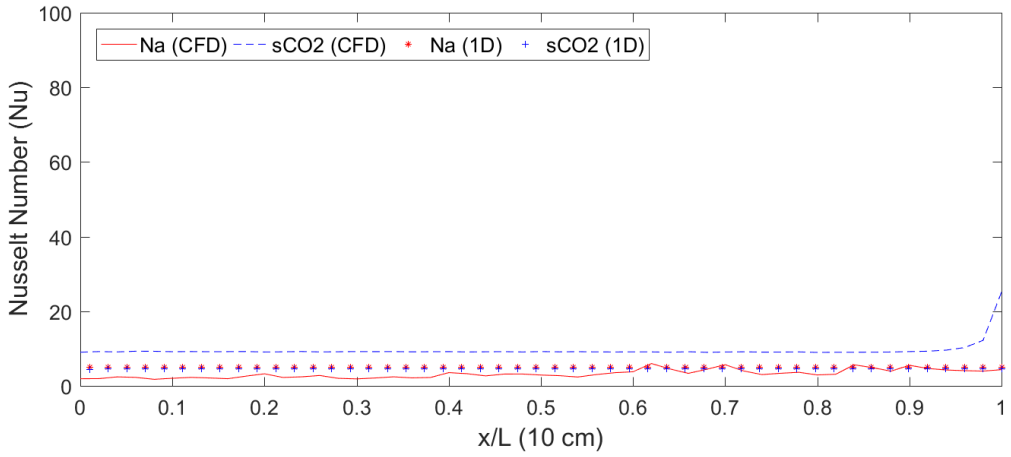

FIGURE 10: Nusselt number profiles for 10 cm length channel with liquid sodium and supercritical CO2 mass flow rate of 1.060e-5 kg/s and 1.07e-5 kg/s respectively. Na Peclet number is 0.086

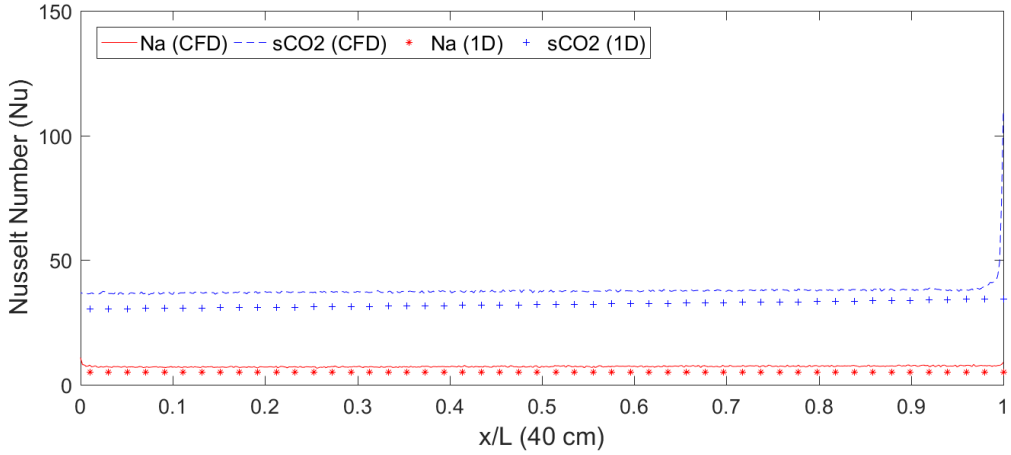

FIGURE 11: Nusselt number profiles for 40 cm length channel with liquid sodium and supercritical CO2 mass flow rate of 1.49e-4 kg/s and 1.51e-4 kg/s respectively. Na Peclet number is 1.2.

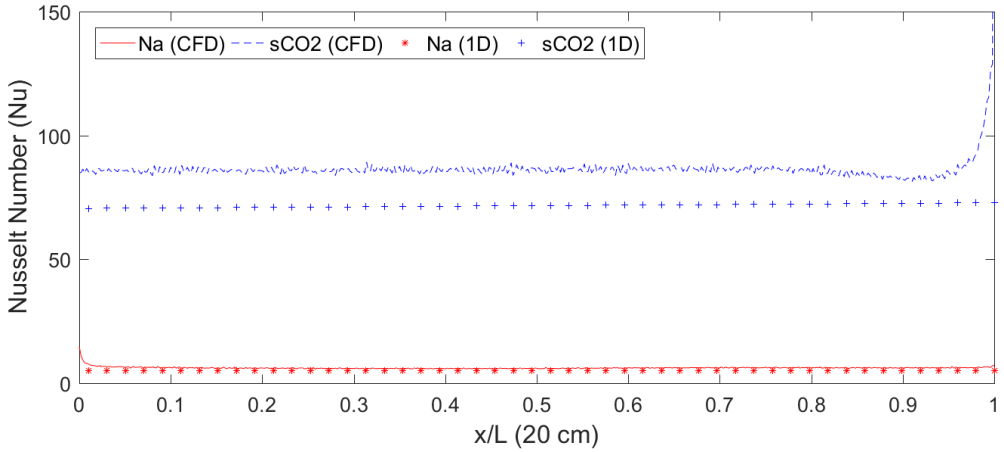

FIGURE 12: Nusselt number profiles for 80 cm length channel with liquid sodium and supercritical CO2 mass flow rate of 1.49e-3 kg/s and 1.52e-3 kg/s respectively. Na Peclet number is 12.

3.3 Effect of Mass Flow Rate Only and Channel Geometry

According to Section 3.1, the effect of axial conduction within sodium is considerably less as the channel length was increased from 10 cm to 40 cm. However, longer channels also accompanied with increase of mass flow rates of the fluids. In this section, the effect of mass flow rate only will be examined first for the 10 cm channel, followed by a preliminary study of channel geometry for thermal-hydraulic optimization. Specifically, wavy channel is compared with the straight channel.

Compared to the simulation results shown Figure 7, the simulation shown in Figure 13 had 10 times of flow rates for both fluids. As expected, the heat transfer effectiveness is significantly decreased from the 85% (1-D model) to 68% (1-D model) or 72% (CFD model). However, with increase in mass flow rate and the associated overall heat transfer rate (although lower effectiveness), the influence of axial conduction within the sodium became insignificant – both models agreed well and captured the similar trend of heat transfer inside the fluids. In this case, a 1-D model without accounting for axial conduction can still be reasonable prediction for Na-sCO2 heat transfer. In addition, the CFD simulation indicated a bigger portion of the fluid channels (10 cm) experienced the entrance length effect associated with the sCO2 side compared the lower flow rate case (Figure 7), which also explains the lower heat transfer effectiveness for the 1-D model as the entrance length effect is not included. As the overall heat transfer

coefficient between sodium and sCO2 is controlled by the sCO2 side, higher convective heat transfer coefficient in the developing flow helped increase heat transfer, i.e. temperature change shown in Figure 13. With further increasing of the mass flow rates to 80 times of the basic flow, the heat transfer effectiveness continued to become lower with 50% (1-D model) and 57% (CFD model). As shown in Figure 14, the same trend observed for 10X flow shown in Figure 13 also preserved. Similar difference between the 1D and CFD models is also repeated with CFD model outperformed the 1-D model.

Given the low heat transfer characteristics for sCO2 and the potential axial conduction effect, an exploratory study was carried out to investigate and ultimately optimize channel geometries for overall thermal-hydraulic performance of Na-sCO2 intermediary heat exchangers. The preliminary result for a wavy channel is presented in Figure 15. Compared to the straight channel (10 cm) with 80 times of the basic flow (result shown in Figure 14), significant improvement on the heat transfer effectiveness (66% vs. 57%) was achieved per the CFD simulations. However, this heat transfer improvement came with substantial pressure drop penalty as shown in Fig. 16.

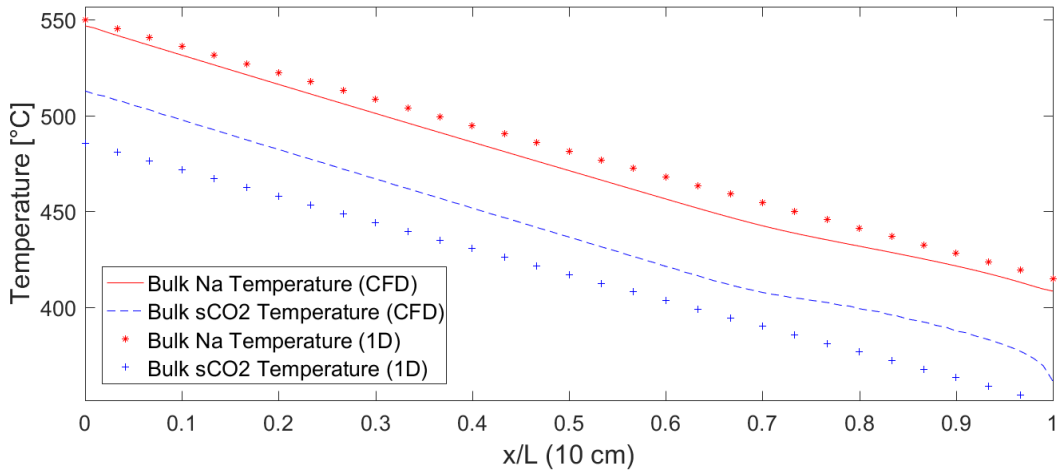

FIGURE 13: Temperature profiles of liquid sodium and supercritical CO2 for 10 cm channel under 10x of the basic flow: Na = 1.060e-5 kg/s and sCO2 = 1.07e-5 kg/s

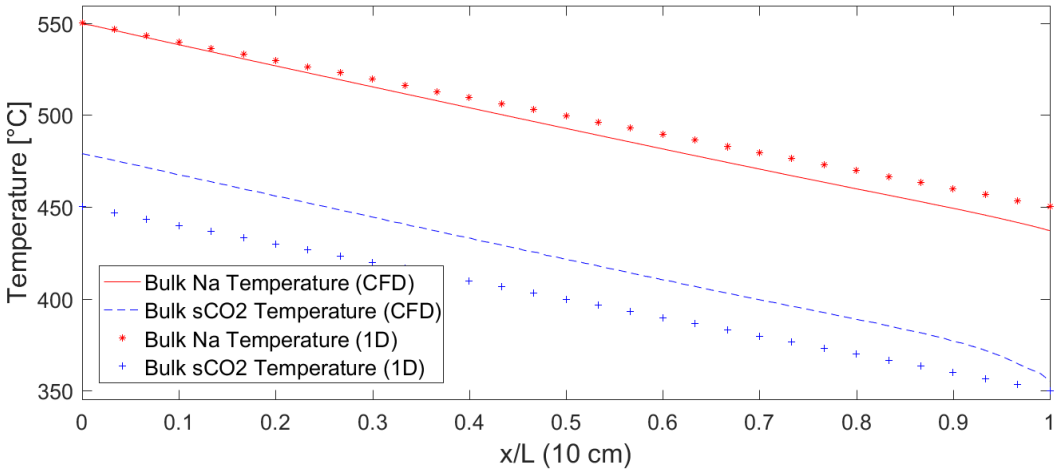

FIGURE 14: Temperature profiles of liquid sodium and supercritical CO2 for 10 cm channel under 80x of the basic flow: Na = 1.060e-5 kg/s and sCO2 = 1.07e-5 kg/s

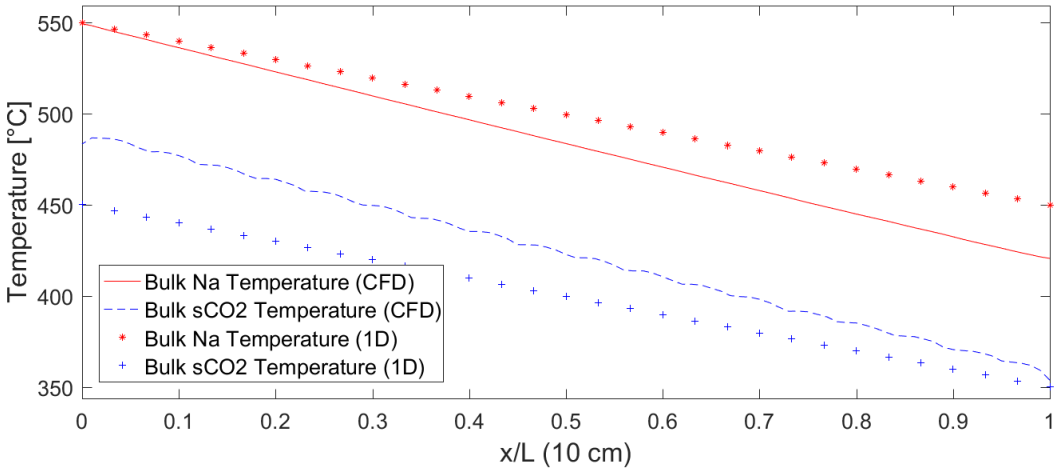

FIGURE 15: Temperature profiles of liquid sodium and supercritical CO2 for 10 cm (**Wavy**) channel under 80x of the basic flow: Na = 1.060e-5 kg/s and sCO2 = 1.07e-5 kg/s

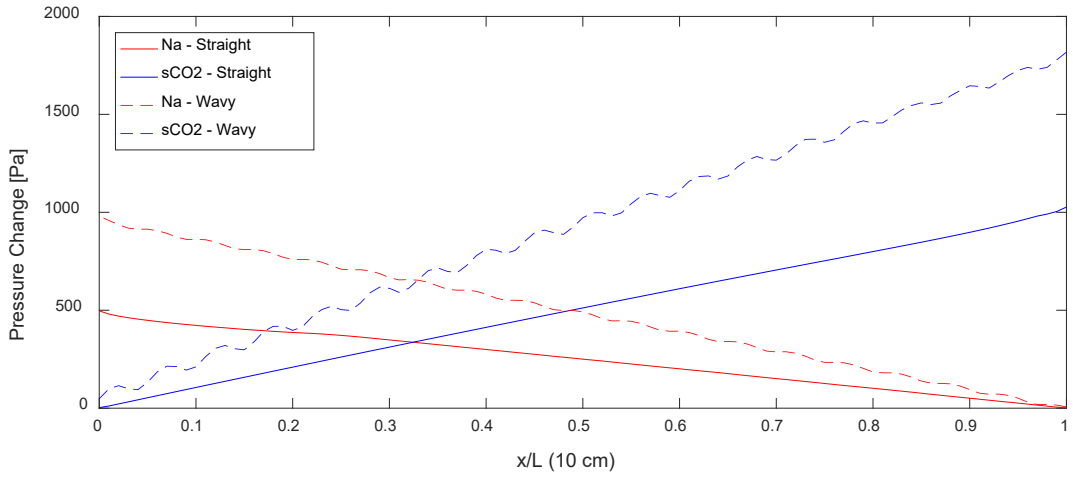

FIGURE 16: Comparison of pressure drops (CFD) between 10 cm straight and wavy channels

3.4 Temperature Contour of Channel Walls

While it is essential to plot the global streamwise bulk fluid temperature profiles, it is also helpful to plot the local temperature contour at a given streamwise location to unveil further insights about local heat transfer between the fluids. Figure 17 provides a snapshot of temperature contour for both the modified Na channel (rectangular) and final Na channel (semi-circle) designs. Figure 17 (left) shows the temperature contour for the 40 cm channel with the cross section located at the midpoint of the heat exchanger channel (20 cm from either end point). It includes the wall temperatures of both Na and sCO2 channels as well as the sodium fluid temperature. As shown, the entire wall temperature only varies by a couple of degrees from the temperature of the sodium. Similarly, Figure 17 (right) shows the wall temperature profile for the final Na channel (semi-circle) design for 10 cm channel simulation when the mass flow rate is 80 times of the basic flow. The cross section is located 1 cm off the sodium inlet. Its profile further illustrates the similar heat transfer characteristics as result of the high thermal conductivity of the sodium. It readily conducts its thermal energy into the metal channel walls, indicating the overall heat transfer process is controlled by sCO2. While not shown in Figure 18 (left), the sCO2 bulk fluid temperature is 437 °C at that location, or about 17 °C lower than the H-CHX wall temperature. For the case shown in Figure 17 (right), the channel wall temperature varies from 528 °C to 539 °C while the

sodium and sCO2 fluid temperatures are at 470 °C and 535 °C, respectively. Both cases indicate again the sCO2 side has the largest thermal resistance thus dominates the heat transfer process.

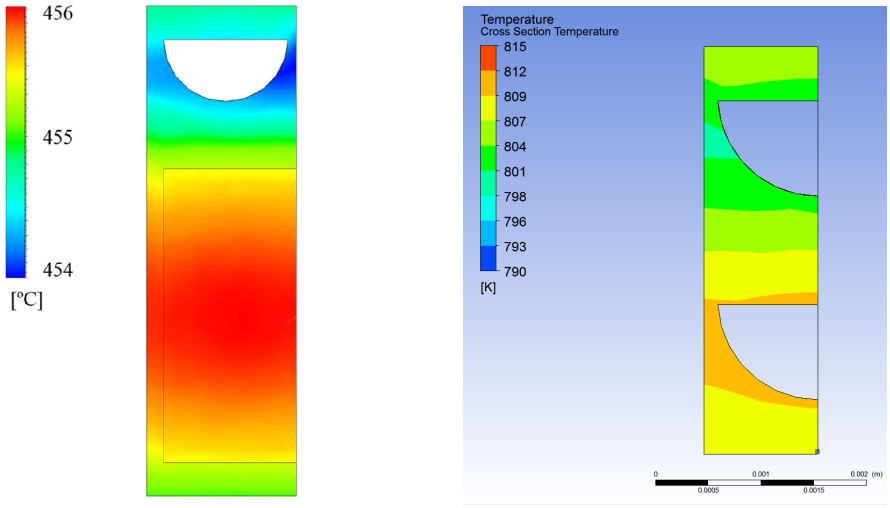

FIGURE 17: (left) Temperature contour plot of the heat exchanger cross-section located at the mid-point of the 40 cm channel; (right) Temperature contour plot of the heat exchanger cross-section located at 1 cm of the sodium inlet for the 10 cm channel

CONCLUSION

With the advent of sodium fast reactor and supercritical CO2 technologies, achieving timely and improved understanding of sodium-sCO2 heat transfer and designing high-performance hybrid compact heat exchangers (H-CHX) becomes increasingly important. This paper presented three heat transfer models for sodium-sCO2 H-CHX, including the 1-D model, CFD model and Temperature-Jump model. Comparisons of the models were made through simulations of heat exchanger with different channel lengths and mass flow rates. Although sizable deviations between the 1-D and CFD models were observed for the 10-cm length channel due to excessive axial conduction within the sodium, no significant difference was identified for the 40-cm and 80-cm length channels. Increasing mass flow rate also helped reduce the axial conduction effect for the 10-cm length channels. While being slightly underpredicted, the predicted Nusselt numbers by the 1-D model were reasonably closed to the CFD results using a SST k−ω turbulence model while significantly reducing the computational time. Adding the temperature-jump

model was able to capture the sudden temperature jump at the sodium inlet predicted by the CFD simulation after turning off the inlet thermal diffusion, which can help extend the 1-D model for low Peclet Number flows, improving its performance prediction capability.

According to the simulation results, improvement should be focused on increasing heat transfer in the sCO2 side. A preliminary study on wavy channel indicates there is an optimization potential for finding more desirable channel geometry for improved thermal performance. The dramatic increase in pressure drop can be a serious concern, which is warranty of further investigations including experimental validation.

ACKNOWLEDGMENT

The authors are gratefully for the funding support provided by the Department of Energy's NUEP program.

REFERENCES

[1] K. H. Yoon, H.-K. Kim, H. S. Lee, and J. S. Cheon, "Component design and accident analysis of fuel assembly for prototype GEN-IV sodium-cooled fast reactor," *Nucl. Eng. Des.*, vol. 340, pp. 133–145, 2018.
[2] P. Lorusso *et al.*, "GEN-IV LFR development: Status & perspectives," *Prog. Nucl. Energy*, vol. 105, pp. 318–331, 2018.
[3] G. Locatelli, M. Mancini, and N. Todeschini, "Generation IV nuclear reactors: Current status and future prospects," *Energy Policy*, vol. 61, pp. 1503–1520, 2013.
[4] S. Grape, S. J. Svärd, C. Hellesen, P. Jansson, and M. Å. Lindell, "New perspectives on nuclear power—Generation IV nuclear energy systems to strengthen nuclear non-proliferation and support nuclear disarmament," *Energy Policy*, vol. 73, pp. 815–819, 2014.
[5] H. Ohshima and S. Kubo, "5 - Sodium-cooled fast reactor," in *Handbook of Generation IV Nuclear Reactors*, I. L. Pioro, Ed. Woodhead Publishing, 2016, pp. 97–118.
[6] E. L. Zebroski, "Fast reactor designs in the USA: changing goals and options," *Energy*, vol. 23, no. 7, pp. 533–548, 1998.
[7] M. Simnad, "Overview of fast breeder reactors," *Energy*, vol. 23, no. 7, pp. 523–531, 1998.
[8] C.-P. Zaleski, "Overview of future development of fast neutron reactors," *Energy*, vol. 23, no. 7, pp. 571–579, 1998.
[9] C.-P. Zaleski and E. L. Zebroski, "Options for further developments of fast reactors," *Energy*, vol. 23, no. 7, pp. 549–569, 1998.
[10] K. Aoto *et al.*, "A summary of sodium-cooled fast reactor development," *Prog. Nucl. Energy*, vol. 77, pp. 247–265, 2014.

[11] P. Song *et al.*, “Numerical approach to study the thermal-hydraulic characteristics of Reactor Vessel Cooling system in sodium-cooled fast reactors,” *Prog. Nucl. Energy*, vol. 110, pp. 213–223, 2019.
[12] T. Sumner, A. Moisseytsev, J. Sienicki, and F. Heidet, “Safety analysis of the FASt TEst reactor (FASTER) preconceptual design,” *Prog. Nucl. Energy*, vol. 108, pp. 454–464, 2018.
[13] B. Merk, A. Stanculescu, P. Chellapandi, and R. Hill, “Progress in reliability of fast reactor operation and new trends to increased inherent safety,” *Appl. Energy*, vol. 147, pp. 104–116, 2015.
[14] H.-Y. Jung, J. I. Lee, M.-H. Wi, and H. J. Ahn, “An investigation of sodium–CO2 interaction byproduct cleaning agent for SFR coupled with S-CO2 Brayton cycle,” *Nucl. Eng. Des.*, vol. 297, pp. 158–165, 2016.
[15] T. Fanning, “‘Sodium as a Fast Reactor Coolant’. In Topical seminar series on sodium fast reactors, Argonne National Laboratory, U.S. Department of Energy. 2017.” Argonne National Laboratory, DOE, 2017.
[16] Z. Qiu, Z. Ma, Y. Wu, S. Qiu, and G. Su, “Experimental research on the thermal hydraulic characteristics of liquid sodium flowing in annuli with low Peclet number,” *Ann. Nucl. Energy*, vol. 75, pp. 483–491, 2015.
[17] Y. Wu *et al.*, “Review on heat transfer and flow characteristics of liquid sodium (1): Single-phase,” *Prog. Nucl. Energy*, vol. 104, pp. 306–316, 2018.
[18] K. Aoto *et al.*, “A summary of sodium-cooled fast reactor development,” *Prog. Nucl. Energy*, vol. 77, pp. 247–265, 2014.
[19] F. Alcántara-Ávila, S. Hoyas, and M. J. Pérez-Quiles, “DNS of thermal channel flow up to Reτ=2000 for medium to low Prandtl numbers,” *Int. J. Heat Mass Transf.*, vol. 127, pp. 349–361, 2018.
[20] I. Tiselj and L. Cizelj, “DNS of turbulent channel flow with conjugate heat transfer at Prandtl number 0.01,” *Nucl. Eng. Des.*, vol. 253, pp. 153–160, 2012.
[21] L. Bricteux, M. Duponcheel, G. Winckelmans, I. Tiselj, and Y. Bartosiewicz, “Direct and large eddy simulation of turbulent heat transfer at very low Prandtl number: Application to lead–bismuth flows,” *Nucl. Eng. Des.*, vol. 246, pp. 91–97, 2012.
[22] M. Duponcheel, L. Bricteux, M. Manconi, G. Winckelmans, and Y. Bartosiewicz, “Assessment of RANS and improved near-wall modeling for forced convection at low Prandtl numbers based on LES up to Reτ=2000,” *Int. J. Heat Mass Transf.*, vol. 75, pp. 470–482, 2014.
[23] G. Grötzbach, “Challenges in low-Prandtl number heat transfer simulation and modelling,” *Nucl. Eng. Des.*, vol. 264, pp. 41–55, 2013.
[24] A. Shams, A. D. Santis, L. K. Koloszar, A. V. Ortiz, and C. Narayanan, “Status and perspectives of turbulent heat transfer modelling in low-Prandtl number fluids,” *Nucl. Eng. Des.*, vol. 353, p. 110220, 2019.
[25] M. Aminuddin and S. M. Zubair, “Analytical solutions to counter-flow heat exchanger subjected to external heat flux and axial conduction,” *Int. J. Refrig.*, vol. 74, pp. 22–37, 2017.
[26] M. Vera and A. E. Quintero, “On the role of axial wall conduction in mini/micro counterflow heat exchangers,” *Int. J. Heat Mass Transf.*, vol. 116, pp. 840–857, 2018.
[27] A. Parahovnik, N. Tzabar, Y. Haas, L. Parahovnik, I. Rosinsky, and G. Yossifon, “Evaluation of axial conduction effects and heat losses in counter-flow microscale heat exchangers,” *Appl. Therm. Eng.*, vol. 121, pp. 1095–1101, 2017.
[28] L. Santini, C. Accornero, and A. Cioncolini, “On the adoption of carbon dioxide thermodynamic cycles for nuclear power conversion: A case study applied to Mochovce 3 Nuclear Power Plant,” *Appl. Energy*, vol. 181, pp. 446–463, 2016.
[29] H. S. Pham *et al.*, “Mapping of the thermodynamic performance of the supercritical CO2 cycle and optimisation for a small modular reactor and a sodium-cooled fast reactor,” *Energy*, vol. 87, pp. 412–424, 2015.

[30] D. Vivaldi, F. Gruy, and C. Perrais, “A numerical model for the CO2–sodium chemical interactions in Sodium Fast nuclear Reactors,” *Chem. Eng. Res. Des.*, vol. 96, pp. 121–129, 2015.
[31] B. S. Oh *et al.*, “Safety evaluation of supercritical CO2 cooled micro modular reactor,” *Ann. Nucl. Energy*, vol. 110, pp. 1202–1216, 2017.
[32] H. A. Muhammad, G. Lee, J. Cho, U. H. Bhatti, Y.-J. Baik, and B. Lee, “Design and optimization of CO2 pressurization system integrated with a supercritical CO2 power cycle for the CO2 capture and storage system,” *Energy Convers. Manag.*, vol. 195, pp. 609–619, 2019.
[33] J. H. Park, H. S. Park, J. G. Kwon, T. H. Kim, and M. H. Kim, “Optimization and thermodynamic analysis of supercritical CO2 Brayton recompression cycle for various small modular reactors,” *Energy*, vol. 160, pp. 520–535, 2018.
[34] J. Y. Heo, M. S. Kim, S. Baik, S. J. Bae, and J. I. Lee, “Thermodynamic study of supercritical CO2 Brayton cycle using an isothermal compressor,” *Appl. Energy*, vol. 206, pp. 1118–1130, 2017.
[35] Y. Ma, T. Morozyuk, M. Liu, J. Yan, and J. Liu, “Optimal integration of recompression supercritical CO2 Brayton cycle with main compression intercooling in solar power tower system based on exergoeconomic approach,” *Appl. Energy*, vol. 242, pp. 1134–1154, 2019.
[36] M. Noaman, G. Saade, T. Morosuk, and G. Tsatsaronis, “Exergoeconomic analysis applied to supercritical CO2 power systems,” *Energy*, vol. 183, pp. 756–765, 2019.
[37] H. Li *et al.*, “Preliminary design assessment of supercritical CO2 cycle for commercial scale coal-fired power plants,” *Appl. Therm. Eng.*, vol. 158, p. 113785, 2019.
[38] Z. Ren, C.-R. Zhao, P.-X. Jiang, and H.-L. Bo, “Investigation on local convection heat transfer of supercritical CO2 during cooling in horizontal semicircular channels of printed circuit heat exchanger,” *Appl. Therm. Eng.*, vol. 157, p. 113697, 2019.
[39] H. Li *et al.*, “Development of a new forced convection heat transfer correlation for CO2 in both heating and cooling modes at supercritical pressures,” *Int. J. Therm. Sci.*, vol. 50, no. 12, pp. 2430–2442, 2011.
[40] Y. Lei and Z. Chen, “Numerical study on cooling heat transfer and pressure drop of supercritical CO2 in wavy microchannels,” *Int. J. Refrig.*, vol. 90, pp. 46–57, 2018.
[41] Z. Yang, W. Chen, and M. K. Chyu, “Numerical study on the heat transfer enhancement of supercritical CO2 in vertical ribbed tubes,” *Appl. Therm. Eng.*, vol. 145, pp. 705–715, 2018.
[42] M. Saeed and M.-H. Kim, “Thermal-hydraulic analysis of sinusoidal fin-based printed circuit heat exchangers for supercritical CO2 Brayton cycle,” *Energy Convers. Manag.*, vol. 193, pp. 124–139, 2019.
[43] J. Khalesi and N. Sarunac, “Numerical analysis of flow and conjugate heat transfer for supercritical CO2 and liquid sodium in square microchannels,” *Int. J. Heat Mass Transf.*, vol. 132, pp. 1187–1199, 2019.
[44] Y. Zhang, M. Peng, G. Xia, and T. Cong, “Numerical investigation on local heat transfer characteristics of S-CO2 in horizontal semicircular microtube,” *Appl. Therm. Eng.*, vol. 154, pp. 380–392, 2019.
[45] Y. Zhu, Y. Huang, S. Lin, C. Li, and P. Jiang, “Study of convection heat transfer of CO2 at supercritical pressures during cooling in fluted tube-in-tube heat exchangers,” *Int. J. Refrig.*, vol. 104, pp. 161–170, 2019.
[46] L. Chai and S. A. Tassou, “Effect of cross-section geometry on the thermohydraulic characteristics of supercritical CO2 in minichannels,” *Energy Procedia*, vol. 161, pp. 446–453, 2019.
[47] X. Zhang, et al., “Compact Heat Exchanger Design and Testing for Advanced Reactors and Advanced Power Cycles.” Final Report, DOE NEUP, 2018.
[48] Cha, J. E., et al., “Development of a Supercritical CO2 Brayton Energy Conversion System Coupled with a Sodium Cooled Fast Reactor,” *Nucl. Eng. Technol.*, vol. 41, no. 8, pp. 1025–1044.
[49] Nestell, J. and T. L. Sham, “ASME Code Considerations for the Compact Heat Ex changer.” 2015.

[50] Renaud Le Pierres, D. Southall, S. Osborne, “Impact of Mechnaical Design Issues on Printed Circuit Heat Exchangers,” in *sCO2 Power Cycle Symposium*, 2011.
[51] Ishizuka, T. et al., “Thermal-Hydraulic Characteristics of a Printed Circuit Heat Exchanger in a Supercritical CO2 Loop,” presented at the The 11th International Topical Meeting on Nu- clear Reactor Thermal-Hydraulics, 2016.
[52] R. Shah and A. London, *Laminar Flow Forced Convection in Ducts*. 1978.
[53] S. H. Yoon, J. H. Kim, Y. W. Hwang, M. S. Kim, K. Min, and Y. Kim, “Heat transfer and pressure drop characteristics during the in-tube cooling process of carbon dioxide in the supercritical region,” *Int. J. Refrig.*, vol. 26, no. 8, pp. 857–864, 2003.
[54] R. Seban and A. Shimazaki, “Heat Transfer to a fluid flowing turbulently in a smooth pipe with walls at constant temperature,” *In: Paper No. 50-A-128, ASME.*
[55] H. Li, Y. Zhang, L. Zhang, M. Yao, A. Kruizenga, and M. Anderson, “PDF-based modeling on the turbulent convection heat transfer of supercritical CO2 in the printed circuit heat exchangers for the supercritical CO2 Brayton cycle,” *Int. J. Heat Mass Transf.*, vol. 98, pp. 204–218, 2016.
[56] M. Marchionni, L. Chai, G. Bianchi, and S. A. Tassou, “Numerical modelling and performance maps of a printed circuit heat exchanger for use as recuperator in supercritical CO2 power cycles,” *Energy Procedia*, vol. 161, pp. 472–479, 2019.
[57] “NIST Standard Reference Database 23 - NIST Reference Thermodynamics and Transport Properties.” 2016.
[58] Fink, J. and Leibowitz, L., “Thermodynamic and Transport Properties of Sodium Liquid and Vapor.” 1995.
[59] “Procedure for Estimation and Reporting of Uncertainty Due to Discretization in CFD Applications,” *J. Fluids Eng.*, vol. 130, no. 7, p. 078001.